

Energy shielding by cavitation bubble clouds in burst wave lithotripsy

Kazuki Maeda,^{1,a)} Adam D. Maxwell,^{2,b)} Tim Colonius,¹ Wayne Kreider,²
 and Michael R. Bailey^{2,b)}

¹*Division of Engineering and Applied Science, California Institute of Technology, 1200 East California Boulevard, Pasadena, California 91125, USA*

²*Center for Industrial and Medical Ultrasound, Applied Physics Laboratory, University of Washington, 1013 Northeast 40th Street, Seattle, Washington 98105, USA*

(Received 20 August 2018; revised 30 October 2018; accepted 31 October 2018; published online 26 November 2018)

Combined laboratory experiment and numerical simulation are conducted on bubble clouds nucleated on the surface of a model kidney stone to quantify the energy shielding of the stone caused by cavitation during burst wave lithotripsy (BWL). In the experiment, the bubble clouds are visualized and bubble-scattered acoustics are measured. In the simulation, a compressible, multi-component flow solver is used to capture complex interactions among cavitation bubbles, the stone, and the burst wave. Quantitative agreement is confirmed between results of the experiment and the simulation. In the simulation, a significant shielding of incident wave energy by the bubble clouds is quantified. The magnitude of shielding can reach up to 90% of the energy of the incoming burst wave that otherwise would be transmitted into the stone, suggesting a potential loss of efficacy of stone comminution. There is a strong correlation between the magnitude of the energy shielding and the amplitude of the bubble-scattered acoustics, independent of the initial size and the void fraction of the bubble cloud within a range addressed in the simulation. This correlation could provide for real-time monitoring of cavitation activity in BWL. © 2018 Acoustical Society of America.

<https://doi.org/10.1121/1.5079641>

[CCC]

Pages: 2952–2961

I. INTRODUCTION

Cavitation bubble clouds nucleated in the human body during the passage of tensile components of acoustic waves are of critical importance for the safety and efficacy of the treatment of lithotripsy (Coleman *et al.*, 1987; Ikeda *et al.*, 2006; Lingeman *et al.*, 2009; Miller *et al.*, 2012; Pishchalnikov *et al.*, 2003; Stride and Coussios, 2010; Tanguay, 2004). Shock wave lithotripsy (SWL) uses a shock waveform of pulses with a peak amplitude of $O(10\text{--}100)$ MPa. The strong tensile tail results in the formation of a large bubble cluster that can violently collapse to cause tissue injury and enhance stone comminution, the former of which has been seen as a major limitation of SWL (Bailey *et al.*, 2006; Evan *et al.*, 2002; McAteer *et al.*, 2005). Burst wave lithotripsy (BWL) is an alternative to SWL and uses high-intensity, focused ultrasound in the form of $O(10)$ cycles at an amplitude of $O(1\text{--}10)$ MPa and a frequency of $O(100)$ kHz for stone comminution (Maxwell *et al.*, 2015; Thoma, 2014). Due to the low peak amplitude of the wave, resulting cloud cavitation in BWL is expected to involve smaller bubbles and consequently less violent bubble dynamics. A recent experimental study *in vitro* has shown that cavitation bubble clouds with a size of $O(1)$ mm are

formed during a passage of the burst wave (Maeda *et al.*, 2015). A subsequent study has shown that the bubble clouds can scatter a large portion of incident wave and reduce the wave energy further downstream (Maeda and Colonius, 2018a). Therefore, it has been hypothesized that the bubble clouds in BWL may cause energy shielding of nearby kidney stones. The energy shielding could lower the efficacy of stone comminution, and thus it is desirable to characterize the process as a function of the incident wave and expected size and number of bubble nuclei.

To investigate this phenomenon, we study bubble clouds nucleated on the surface of an epoxy stone model during the passage of a burst wave by a medical transducer in water through combined experimental measurements *in vitro* and companion numerical simulations. In the experiment, we visualize the evolution of bubble clouds using a high-speed camera and measure the backscattered acoustics from the bubbles with the transducer array elements. In the simulation, we combine numerical methods for modeling compressible, multi-component flows to capture complex interactions among bubbles, the stone, and the burst wave. Simulated evolution of the bubble cloud and the bubble scattered acoustics quantitatively agree with the results of the experiment. In the simulation, we vary the initial void fraction and the size of bubble cloud to assess the magnitude of the shielding as well as its correlation with the bubble-scattered acoustics. Results indicate that the magnitude of the shielding reaches up to 90% of the energy of the incident burst wave that otherwise transmits into the stone. We

^{a)}Current address: Department of Mechanical Engineering, University of Washington, Seattle, WA 98195, USA. Electronic mail: kazuki.e.maeda@gmail.com

^{b)}Also at: Department of Urology, University of Washington School of Medicine, 1959 Northeast Pacific Street, Seattle, WA 98195, USA.

further discover a strong correlation between the magnitude of the shielding and the amplitude of the backscattered acoustics, independent of the initial condition of the cloud. These results can be used to further identify appropriate parameters and improve the efficacy of stone comminution in BWL.

II. EXPERIMENTAL SETUP

Figure 1(a) shows a schematic of the experimental setup. We generate pulses of ten cycles of a sinusoidal pressure wave with a frequency of 340 kHz and a peak maximum focal pressure of 7.0 MPa from a multi-element array focused transducer with an aperture of 180 mm and focal length of 150 mm [Fig. 1(b)] toward a cylindrical shape of epoxy stone model with its axis aligned on the acoustic axis of the transducer. The transducer is composed of 18 circular elements made from a ring-shaped piezo-ceramic plate with an outer diameter of 38.1 mm and inner diameter of 12.7 mm. Each of the elements is designed to generate a spherical wave front that propagates inward to the center corresponding to the focal point. Further details of the transducer are available elsewhere (Maeda and Colonius, 2017). The pulse repetition frequency (PRF) is 100 Hz. The focal point of the transducer is located at the center of the stone. The height and diameter of the stone are 10 and 6.25 mm, respectively. The water is degassed to approximately 65% O_2 saturation to model the environment of the collecting space of kidney *in vivo* (Chaigneau and Le, 1968; Hwang *et al.*, 1998). This condition contrasts with that used in the initial demonstration of BWL *in vitro* in that water was highly degassed to suppress cavitation (Maxwell *et al.*, 2015). Preliminary experiments identified that a thin layer of bubble cloud is formed on the proximal base of the stone, where the pressure is locally amplified due to reinforcement of the incoming burst wave by the wave reflected by the stone. A high-speed camera is triggered to capture an image of bubble cloud at a specific time during the passage of each pulse. We concurrently sample the backscattered acoustics from the bubble cloud and the stone by using the transducer array elements between the matching network and the transducer.

III. SIMULATION SETUP

A. Numerical methods

In simulations, we formulate the dynamics of the multi-component mixture using the compressible, multi-component, Navier-Stokes equation. We model the stone as an isotropic, elastic solid with a bulk modulus of $K = 7.14$ GPa and a density of $\rho_s = 1200$ kgm $^{-3}$. The values of the modulus and the density are chosen as those of the epoxy resin used for the experimental stone model. The shear modulus is set to zero. The longitudinal sound speed is $\sqrt{(K/\rho_s)} = 2440$ ms $^{-1}$. We neglect the viscosity of the stone; the acoustic attenuation in the epoxy resin is smaller than 1 dB/cm and negligible for results considered in the present study. This modeling is equivalent to assume that the stone is an inviscid, compressible fluid with the same values of the modulus and the density. The coupled dynamics of the stone and the surrounding water are modeled using an interface capturing method (Coralic and Colonius, 2014; Perigaud and Saurel, 2005). The interface of the stone is modeled as a sharp, but continuous region of mixture of water and the stone. The acoustic impedance mismatch at the interface is accurately modeled for pressure waves with a wavelength larger than the grid resolution. The bubbles are assumed to be spherical and fully immersed in water with a certain distance from the stone (bubble are not attached on the stone). For modeling the dynamics of the bubble cloud excited in an ultrasound field, we use an Eulerian-Lagrangian method. The method is derived and validated in detail in Maeda and Colonius (2018b), and applied to parametric simulation of the dynamics of spherical bubble clouds excited by burst waves (Maeda and Colonius, 2018a). We provide a brief summary of the method here. In the method, we describe the dynamics of bubbly mixture using volume-averaged equations of motion (Biesheuvel and vanWijngaarden, 1984; Commander and Prosperetti, 1989; Fuster and Colonius, 2011; Kameda and Matsumoto, 1996)

$$\frac{\partial \bar{p}}{\partial t} + \nabla(\bar{\rho} \bar{u}) = 0, \quad (1)$$

$$\frac{\partial(\bar{\rho} \bar{u})}{\partial t} + \nabla(\bar{\rho} \bar{u} \otimes \bar{u} + p \mathcal{I} - \mathcal{T}) = 0, \quad (2)$$

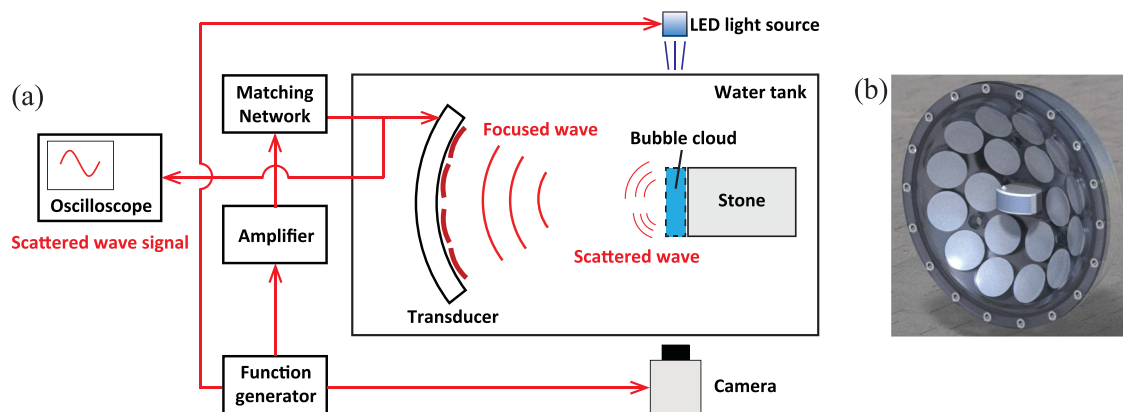


FIG. 1. (Color online) (a) Schematic of the experimental setup. (b) Multi-element array medical transducer (same as that modeled in Sec. II).

$$\frac{\partial \bar{E}}{\partial t} + \nabla \cdot ((\bar{E} + p)\bar{\mathbf{u}} - \mathcal{T} \cdot \bar{\mathbf{u}}) = 0, \quad (3)$$

where ρ is the density, $\mathbf{u} = (u, v, w)^T$ is the velocity, p is the pressure and E is the total energy. $\overline{(\cdot)}$ denotes the volume averaging operator that acts on arbitrary field variables (\cdot) : $\overline{(\cdot)} = (1 - \beta)(\cdot)_l + \beta(\cdot)_g$, where $\beta \in [0, 1]$ is the volume fraction of gas (void fraction), and subscripts l and g denote the liquid and gas phase, respectively. \mathcal{T} is the effective viscous stress tensor of the mixture, which we approximate as that of the liquid phase: $\mathcal{T} \approx \mathcal{T}_l$. We invoke two approximations valid at the limit of low void fraction: the density of the mixture is approximated by that of the liquid: $\bar{\rho} \approx (1 - \beta)\rho_l$; the slip velocity between the two phases is zero: $\bar{\mathbf{u}} \approx \mathbf{u}_l = \mathbf{u}_g$.

Equations (1)–(3) can then be rewritten as conservation equations in terms of the mass, momentum, and energy of the liquid with source terms as an inhomogeneous hyperbolic system

$$\frac{\partial \mathbf{q}_l}{\partial t} + \nabla \cdot \mathbf{f}(\mathbf{q}_l) = \mathbf{g}(\mathbf{q}_l, \beta, \dot{\beta}), \quad (4)$$

where

$$\mathbf{q}_l = [\rho_l, \rho_l \mathbf{u}_l, E_l]^T, \quad (5)$$

$$\mathbf{f} = [\rho_l \mathbf{u}_l, \rho_l \mathbf{u}_l \otimes \mathbf{u}_l + p\mathcal{I} - \mathcal{T}_l, (E_l + p)\mathbf{u}_l - \mathcal{T}_l \cdot \mathbf{u}_l]^T, \quad (6)$$

and

$$\mathbf{g} = \frac{1}{1 - \beta} \frac{d\beta}{dt} \mathbf{q}_l - \frac{\beta}{1 - \beta} \nabla \cdot (\mathbf{f} - \mathbf{u}_l \mathbf{q}_l). \quad (7)$$

For a thermodynamic closure for the liquid, we employ a stiffened gas equation of state

$$p = (\gamma - 1)\rho\varepsilon - \gamma\pi_\infty, \quad (8)$$

where ε is the internal energy of liquid, γ is the specific heat ratio, and π_∞ is the stiffness. In the present study we use $\gamma = 7.1$ and $\pi_\infty = 3.06 \times 10^8$ Pa for water.

To model the gas phase, we employ a Lagrangian point-bubble approach in that the gas is treated as spherical, radially oscillating cavities consisting of a non-condensable gas and liquid vapor. The center of n th bubble ($n \in \mathbb{Z} : n \in [1, N]$), with a radius of R_n and a radial velocity of \dot{R}_n , is initially defined at the coordinate \mathbf{x}_n and tracked as Lagrangian points during simulations. To define the continuous field of the void fraction in the mixture at coordinate \mathbf{x} , we smear the volume of bubble using a regularization kernel δ

$$\beta(\mathbf{x}) = \sum_{n=1}^N V_n(R_n) \delta(d_n), \quad (9)$$

where V_n is the volume of bubble n , $V_n = 4\pi/3 R_n^3$, and d_n is the distance of the coordinate \mathbf{x} from the center of the bubble, $d_n = |\mathbf{x} - \mathbf{x}_n|$. For numerical representation, we discretize Eq. (4) on an axisymmetric grid and spatially integrate using a fifth-order finite volume WENO scheme

(Coralic and Colonius, 2014). A fourth/fifth-order Runge-Kutta-Cash-Karp (RKCK) algorithm (Cash and Karp, 1990) is employed for time integration of solutions.

To model the dynamics of volumetric oscillations of bubbles, we employ the Keller–Miksis equation (Keller and Miksis, 1980)

$$\begin{aligned} & \left(R_n \left(1 - \frac{\dot{R}_n}{c} \right) \right) \ddot{R}_n + \frac{3}{2} \dot{R}_n^2 \left(1 - \frac{\dot{R}_n}{3c} \right) \\ &= \frac{p_n - p_\infty}{\rho} \left(1 + \frac{\dot{R}_n}{c} \right) + \frac{R_n \dot{p}_n}{\rho c}, \end{aligned} \quad (10)$$

$$p_n = p_{Bn} - \frac{4\mu_l \dot{R}_n}{R_n} - \frac{2\sigma}{R_n}, \quad (11)$$

where p_n is the pressure at the bubble wall, p_{Bn} is the pressure inside the bubble, σ is the surface tension, and p_∞ is the component of the pressure that forces the radial oscillations of the bubble. We use a reduced-order model to account for heat and mass transfer across the bubble–liquid interface (Preston *et al.*, 2007). In principle, various similar reduced order models for heat and mass transfer can be instead used (Bergamasco and Fuster, 2017; Okita *et al.*, 2013), while the choice of the model would not largely affect the results obtained in this study.

The grid size is uniform with a radial and axial width of $100 \mu\text{m}$ in the stone-wave interaction region. We randomly distribute spherical bubble nuclei with a radius of $10 \mu\text{m}$ in the cylindrical region with the thickness h and the void fraction β_0 , which faces the proximal base of the stone at the initial condition, then track the radial evolution of the bubbles at the sub-grid scale and resolve the bubble-scattered acoustics on the grid. The parameters are chosen as discussed below.

B. Modeling parameters

We model the transducer arrays used in the experiment as a portion of a spherical surface with an aperture of 60 mm and a radius of 50 mm with its center located at the origin. In order to generate focused ultrasound waves from the source surface, we utilize a source-term approach (Maeda and Colonius, 2017). The method can generate unidirectional acoustic waves from a surface of arbitrary geometry, in this case the spherical source surface, by forcing Eq. (4) on the surface in a simulation domain.

For accurate simulation of the bubble dynamics, we calibrate the acoustic source model using experimental measurements. With the input of N_c cycles of a sinusoidal voltage, the output of the transducer is modeled by the following formula:

$$\begin{aligned} p_{\text{trans}} &= p_a \cos(2\pi f t) \\ &\times \left[(1 - e^{-t/\tau_u}) - (1 - e^{-(t - N_c/f)/\tau_d}) H\left(t - \frac{N_c}{f}\right) \right], \end{aligned} \quad (12)$$

where τ_u and τ_d are the ring-up and ring-down times, respectively. In the simulations of focused waves, we excite this

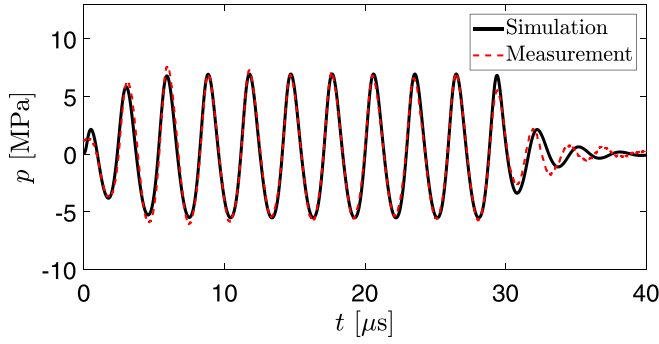


FIG. 2. (Color online) Evolution of the focal pressure obtained in the experiment and the simulation without stone.

expression of the pressure at the source plane, with $\tau_u = 1.5$ and $\tau_d = 2.5 \mu\text{s}$.

In Fig. 2 we compare the evolution of the focal pressure during the passage of the burst wave obtained from the experiment and a simulation without the stone. The head of the wave arrives at the focal point at $t=0$. The simulated waveform and the peak pressure agree well with those of the measurement, except for the period of small oscillations due to ring down after $t=30 \mu\text{s}$. In both the experiment and simulation, the peak negative pressure is -5.5 MPa . The discrepancy between the amplitudes of the peak positive (7.0 MPa) and the peak negative pressures is due to nonlinear distortion of the burst wave. In simulation, we capture the evolution of the bubbles and sample the backscattered acoustics at coordinates on the acoustic source surface with polar angles corresponding to the center of the transducer array elements used in the experiment.

In the experiment, we do not precisely know the population, size distribution, and location of bubbles *a priori*. Therefore, we conduct parametric simulations by varying the thickness and the initial void fraction of the cylindrical bubble cloud within ranges of $h \in [0.25, 1.0] \text{ mm}$ and $\beta_0 \in [1.0, 8.0] \times 10^{-5}$, respectively. For reference, we also simulate a case without bubble cloud. The bubbles are initially monodisperse with radii of $R_0 = 10 \mu\text{m}$. For each combination of the thickness and the void fraction of the bubbly layer, we simulate a single realization of the monodisperse bubbles. The ranges of the parameters were chosen based on the experimental observation and the results of the previous studies of the dynamics of a spherical bubble cloud (Maeda, 2018; Maeda and Colonius, 2018a). In the studies, we used the same numerical method to simulate the dynamics of an isolated, spherical bubble cloud that are nucleated during the passage of a burst wave with an amplitude of $O(10) \text{ MPa}$ and a frequency of 335 kHz in water with various values of initial nuclei population and polydispersity. Through the study, we identified that bubble clouds with an initial mean diameter of $10 \mu\text{m}$ can model the dynamics of bubble clouds observed in companion experiments well, regardless of the initial polydispersity. For this reason, we have chosen monodisperse bubble clouds with an initial mean radius of $10 \mu\text{m}$ in the present study.

IV. RESULTS AND DISCUSSION

A. Bubble dynamics

Figure 3 shows pressure contours at different instants in time during the simulation with $h = 0.75 \text{ mm}$ and $\beta_0 = 1.0 \times 10^{-5}$. A burst wave is generated and focused toward the

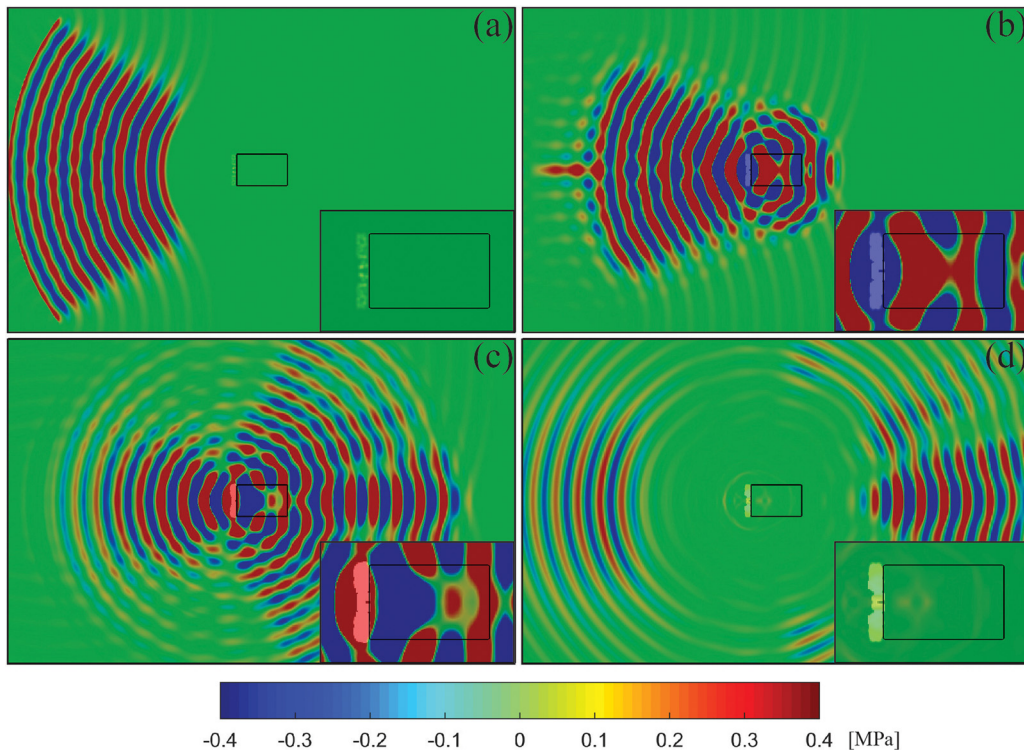


FIG. 3. (Color online) Snapshots of the pressure contour on the axial-plane during the simulation with $h = 1.0 \text{ mm}$ and $\beta_0 = 1.0 \times 10^{-5}$ at (a) $t = -14.7$, (b) 4.5 , (c) 23.7 , and (d) $42.9 \mu\text{s}$. The stone and the void fraction of bubbles are indicated with the black line and by the white shading, respectively. In each image, the inset shows a zoom-in-view of the stone and the bubble cloud.

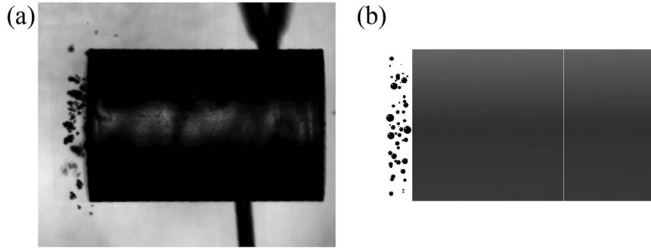


FIG. 4. Images of representative bubble clouds obtained at $t = 35 \mu\text{s}$ from (a) experiment and (b) simulation. The height and diameter of the stone are 10 and 6.25 mm, respectively.

stone [Fig. 3(a)]. A bubble cloud is excited during the passage of the wave [Fig. 3(b)]. A portion of the wave is scattered back from the bubbles and the stone, and the rest of the wave transmits through or around the stone and is scattered forward [Fig. 3(c)]. After the passage of the incident wave, weak reverberation of the pressure wave is observed in the stone [Fig. 3(d)]. Strong collapse of the bubble cloud is not observed. Figure 4 shows representative images of a bubble cloud obtained from the high-speed imaging and the same simulation at $t = 35 \mu\text{s}$. A layer of dispersed bubbles is present on the proximal base of the stone in both images.

In Fig. 5 we compare the evolution of the area occupied by the bubbles projected on a two-dimensional (2D) plane, $A \text{ mm}^2$, obtained in the experimental visualization and the simulation with $h = 0.75 \text{ mm}$ and $\beta_0 = 1.0 \times 10^{-5}$. In the experiment, we converted each image into a binary image by using a post-processing algorithm (Otsu method; Otsu, 1979), and then we count pixels that are occupied by bubbles to compute the area. In the simulation, we output side-view images from the view angle of the high-speed camera [Fig. 4(b)]. We define a 2D Cartesian grid with the same spatial resolution as the high-speed image, and then map the bubbles onto the grid (if a bubble overlaps with a certain cell, we regard the cell as being occupied by the bubble). We then binarize the image in the same way as we did to the experimental image. By doing so, the uncertainties are matched between the experimental image and the snapshots obtained from the simulation. Each data point of the measurement is obtained by averaging 440 independent realizations of the bubble clouds. The uncertainty in the experimental results can be

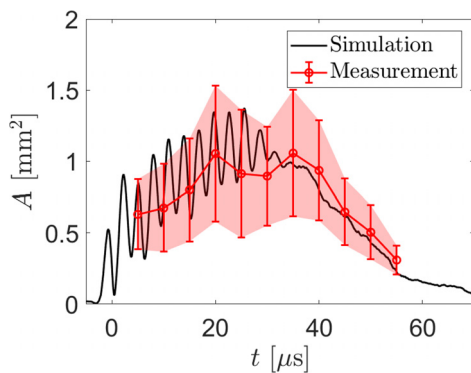


FIG. 5. (Color online) Evolution of the projected area of bubble cloud. Results of the experiment and simulation with $h = 0.75 \text{ mm}$ and $\beta_0 = 1.0 \times 10^{-5}$ are compared. The shaded region corresponds to the standard deviation of the experimental data points.

explained by the stochastic nature of cavitation inception; the location and the number of nuclei on the surface of the stone can fluctuate in excitation by distinct pulses. Nevertheless, we observed statistically consistent behaviors in the bubble clouds over multiple pulses. The result shows that the cloud experiences a transient growth of bubbles with rapid oscillations during the passage of the wave, up to about $t = 30 \mu\text{s}$, followed by a smooth decay. The measurement cannot capture the oscillations, even though they may be present in the experiments, as the sampling frequency is lower than that of the oscillation, while the overall growth to $t = 30 \mu\text{s}$ and subsequent decay after the passage of the wave agree well with the result of the simulation.

Figure 6 shows the projected area of bubbles at $t = 35 \mu\text{s}$ obtained in the simulation as a function of the initial thickness of the bubbly layer. At all values of the initial void fraction, the projected area increases with the thickness. For most cases, the area also increases monotonically with void fraction. At all h , initially dilute bubbly layers tend to grow by a larger factor than dense layers. This can be explained by mutual suppressions of the volumetric growth among bubbles in a dense bubble cloud due to inter-bubble interactions (Maeda and Colonius, 2018a; Wang and Brennen, 1999). The data points are spread over the range of $A \in [0.5, 2] \text{ mm}^2$.

To gain further insight into the bubble dynamics, we take a detailed look at the instantaneous state of bubbles at $t = 35 \mu\text{s}$, as a representative time of the maximal bubble cloud in the experiment and the simulation. Figure 7 shows the probability distribution function (PDF) of the projected area of bubbles obtained from the experiment at $t = 35 \mu\text{s}$. The PDF approximately follows a log-normal distribution. The range of the projected area shown in Fig. 6 covers the wide band of the experimental PDF shown in Fig. 7, within which 92% of the distribution lies. This suggests that the parameters used in the simulation represent the experiment well.

B. Scattered acoustics

In order to quantify the amplitude of the backscattered acoustics, we compute a daylight imaging functional using

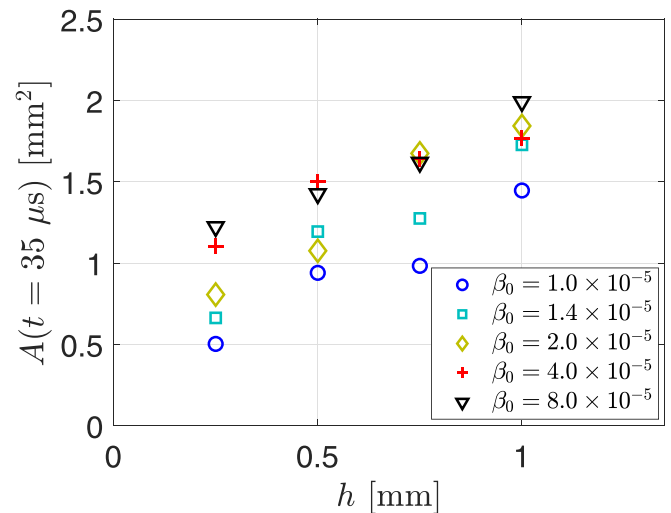


FIG. 6. (Color online) The projected area of bubbles at $t = 35 \mu\text{s}$ as a function of the cloud thickness obtained in the simulation.

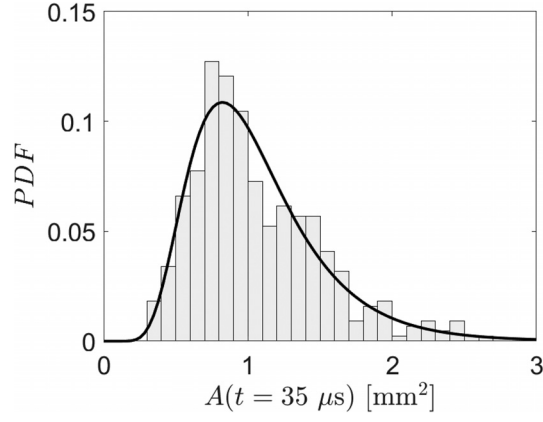


FIG. 7. Probability distribution function (PDF) of the projected area of bubbles obtained in the experiment at $t = 35 \mu s$. Solid line indicates a log-normal fit to the data.

cross correlations from both the experiment and simulations. Given $u(t, \mathbf{x}_i)$, where $i = 1, \dots, N_{\text{sensor}}$, as a set of signals sampled at coordinates \mathbf{x}_i over the time interval $[0, T]$, the cross correlation between signals $u(t, \mathbf{x}_i)$ and $u(t, \mathbf{x}_j)$ is defined as

$$C_T(\tau, \mathbf{x}_j, \mathbf{x}_i) = \frac{1}{T} \int_0^T u(t, \mathbf{x}_i) u(t + \tau, \mathbf{x}_j) dt. \quad (13)$$

Using the cross correlation, the following imaging functional at position \mathbf{z} can be defined as

$$\mathcal{I}(\mathbf{z}) = \sum_{j,l=1}^{N_{\text{sensors}}} C_T^{\text{sym}}(\tau(\mathbf{z}, \mathbf{x}_l) + \tau(\mathbf{z}, \mathbf{x}_j), \mathbf{x}_j, \mathbf{x}_l), \quad (14)$$

where

$$C_T^{\text{sym}}(\tau, \mathbf{x}_j, \mathbf{x}_l) = C_T(\tau, \mathbf{x}_j, \mathbf{x}_l) + C_T(-\tau, \mathbf{x}_j, \mathbf{x}_l). \quad (15)$$

C_T^{sym} is the symmetric component of the cross correlation. Further details of the algorithms used to obtain the functional can be found in [Garnier and Papanicolaou \(2009\)](#).

Figures 8(a) and 8(b) show normalized contours of the tenth power of imaging functional obtained in a representative case from the experiment and the simulation with $h = 0.75 \text{ mm}$ and $\beta_0 = 1.0 \times 10^{-5}$, respectively. Positions with a large value of the imaging functional correspond to estimated locations of the acoustic source. Note that we use the power to visually enhance the contrast in the contours (gamma correction; [Poynton, 2012](#)), while the estimated location of the source is unchanged. In both plots, a region of a large value of the imaging functional is localized within the stone.

Figure 9 shows correlations between the area occupied by the bubbles and the scattering factor at $t = 35 \mu s$. The scattering factor is defined as

$$F = \frac{\max[\mathcal{I}]}{\max[\mathcal{I}_{\text{ref}}]}, \quad (16)$$

where \mathcal{I}_{ref} is the reference value of imaging functional without bubbles. Therefore, F quantifies the enhancement/decay of the scattered acoustics due to the presence of bubbles. Weak positive correlations are observed between the projected area

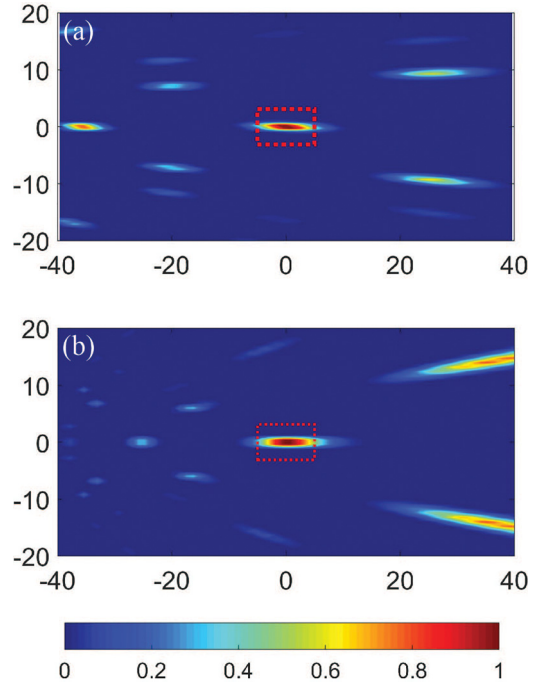


FIG. 8. (Color online) Normalized contour of the tenth power of imaging functional near the focal region obtained from (a) a representative case in the experiment and (b) the simulation with $h = 0.75 \text{ mm}$ and $\beta_0 = 1.0 \times 10^{-5}$. Stones are indicated by dotted lines. The length unit is mm.

and the scattering factor in both the experiment and the simulation. The data points of the simulation show that the scattering is enhanced with the increase in the initial void fraction and the thickness of the bubble cloud. Most of the data points obtained from the simulation lie in the interior of the 92% confidence ellipse obtained from the experimental data points, indicating a good agreement of the scattered acoustics measured in the experiment and that obtained in the simulation.

Notice that in both the experiment and simulation, some data points are in the range of $F < 1$. This indicates that the amplitude of the backscattering is smaller than that without bubble clouds in these cases. This mitigation of the amplitude can be explained by the widening of the scattering angle by the bubble clouds. Without bubbles, the incoming wave tends to get reflected perpendicular to the flat base of the stone, and the scattered wave is most intense opposite the direction of the incident wave. On the other hand, the bubbly layer results in a more omnidirectional scattering. With increasing the thickness and the density of the bubbly layer, thus increasing F , the intensity of the bubble-scattered acoustics becomes enhanced and this realizes $F > 1$.

The good agreement between the experiment and the simulation shown in this section and Sec. IV A suggest that the simulation correctly captures the physics of cavitation near the stone model, and thus can be used to predict quantities inaccessible in the experiment.

C. Energy shielding

In our previous computational study of the dynamics of spherical bubble clouds excited by burst waves, it was shown

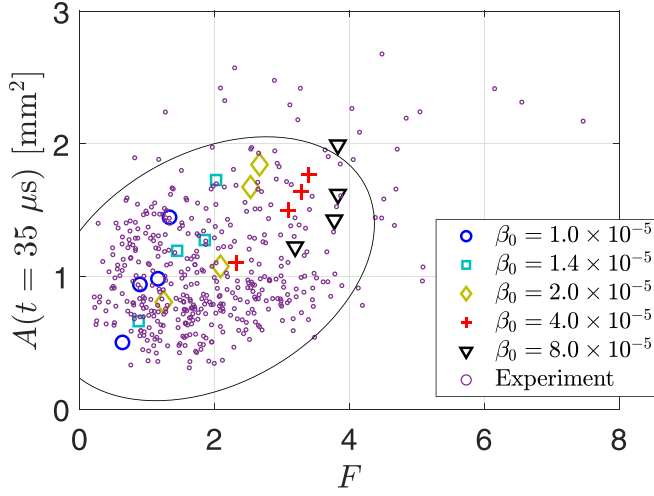


FIG. 9. (Color online) Correlation between the projected area of bubbles at $t = 35 \mu s$ and the scattering factor obtained in both the experiment and the simulation. The black line draws 92% confidence ellipse for the experimental data points.

that the amplitude of the far-field acoustic waves scattered by the cloud and the kinetic energy of liquid induced by the bubble dynamics are strongly correlated (Maeda and Colonius, 2018a). This motivates us in this study to assess correlation between the kinetic energy of the stone excited by the burst wave as a metric of the energy shielding and the imaging functional as a metric of the amplitude of the far-field, scattered acoustics. Direct measurement of the energy in the stone is challenging in the experiment, and thus we compute the quantity by processing the data obtained from the simulation.

Figure 10 shows the evolution of the kinetic energy in the stone, K_{stone} , induced by the burst wave during three distinct cases from the simulations conducted in this study: without bubbles; with the thinnest, initially most dilute cloud ($h = 0.25 \text{ mm}$ and $\beta_0 = 1.0 \times 10^{-5}$); with the thickest, initially densest cloud ($h = 1.0 \text{ mm}$ and $\beta_0 = 8.0 \times 10^{-5}$), where K_{stone} is defined as the kinetic energy of the volume element integrated over the stone

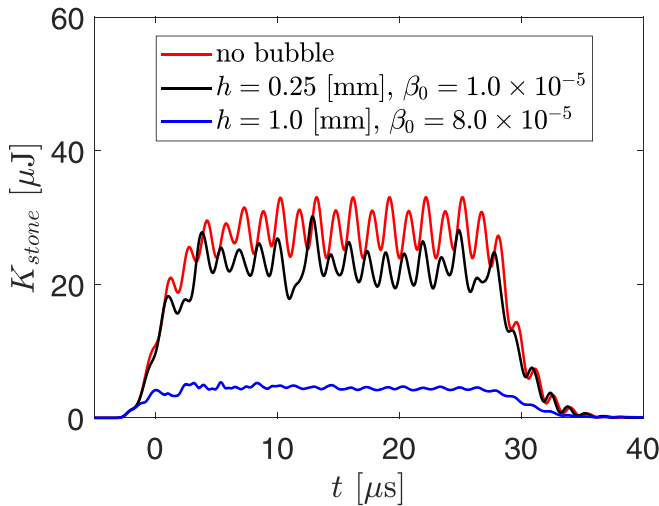


FIG. 10. (Color online) Evolution of the kinetic energy in the stone induced by the burst wave.

$$K_{\text{stone}} = \int_{\text{stone}} \frac{1}{2} \rho u^2 dv. \quad (17)$$

In all the cases, the energy steadily grows after arrival of the wave until around at $t = 10 \mu s$, then oscillates around an average value during the passage of the wave until around $t = 30 \mu s$. After the passage of the wave, the energy steadily decays and reaches zero around $t = 40 \mu s$. The energy is highest for all t when there are no bubbles. The energy level is slightly decreased with the thin and dilute cloud, while it is drastically reduced with the thick and dense cloud. This result indicates that, as might be expected, the energy shielding by bubbles is enhanced by increasing the thickness and/or the void fraction of the cloud.

To quantify the correlation between the shielding and the scattered acoustics, in Fig. 11 we plot the shielding factor S as a function of the scattering factor F . The shielding factor is defined as

$$S = 1 - \frac{P}{P_{\text{ref}}}, \quad (18)$$

where P is the total work done by the acoustic energy to the stone during each simulation: $P = \int K_{\text{stone}} dt$. P_{ref} is the reference value of P obtained in the case without bubbles. Note that $S = 0$ and $S = 1$ indicate no shielding and perfect shielding (no energy transmission into the stone), respectively.

Notably, the plot indicates a strong positive correlation between the shielding factor and the scattering factor over the global range of the data points, independent of the initial condition of bubbles. The shielding factor grows with the increase of the scattering factor and reaches $S \approx 0.9$ at $F \approx 4$. This indicates that the energetic state of the bubble cloud becomes invariant to the initial void fraction and thickness of the layer as they increase. The result indicates that up to 90% of the energy of the incident burst wave can be absorbed/scattered by bubbles that would otherwise be transmitted into the stone.

During the wave propagation, in the experiment, the elastic potential energy and the kinetic energy are excited in

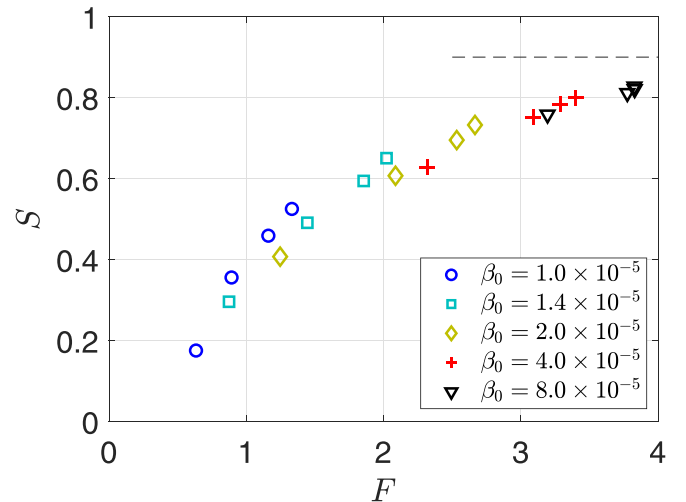


FIG. 11. (Color online) Correlation between the shielding factor and the scattering factor. Dashed line indicates $S = 0.9$.

the stone. The potential energy is composed of the longitudinal and transverse components. For the expression of the potential energy, see, for instance, Landau and Lifshitz (1986). In the present simulation, the transverse component of potential energy is zero since shear stress is not modeled. Nevertheless, the time-averaged kinetic energy in the stone excited by the wave equals that of the total elastic potential energy due to energy conservation, regardless of the magnitude of each component. Therefore, we assume that the kinetic energy is an appropriate metric of the magnitude of the wave energy transmitted into the stone. The present analysis may motivate future work to include modeling of shear stress and the transverse component of the elastic energy as well as their contributions to stone comminution.

D. Implications for BWL

The results of the present study indicate that a thin bubble layer localized on the surface of a stone can reduce transmission of the large portion of incoming wave energy into the stone. This energy shielding could potentially result in loss of efficacy of stone comminution during BWL. This agrees with the hypothesis made in the previous study on the dynamics of isolated, spherical bubble clouds (Maeda and Colonius, 2018a). Though the scattering and/or the shielding effects of bubble clouds excited by shock- and high-intensity focused ultrasound (HIFU) waves have been reported in both numerical and experimental studies (Maxwell *et al.*, 2011; Pishchalnikov *et al.*, 2006; Tanguay, 2004; Yura *et al.*, 2018), to our knowledge, quantification of the effects based on direct comparisons of experiment and corresponding computational fluid dynamics simulation has not been previously made.

The monotonic correlation between the shielding factor and the scattering factor (Fig. 11) suggests that the scattered acoustics can be directly used to estimate the magnitude of the shielding regardless of the bubble dynamics, at least within the range of parameters of bubble clouds addressed in the present study. The energy shielding, thus the activities of cavitation bubbles, could be therefore monitored by ultrasound sensing outside the human body during the treatment of BWL. Such monitoring may enable real-time feedback control of the therapy to optimize the efficacy of stone comminution, for instance, by modulating the wave parameters, including the waveform and the PRF to suppress cavitation for mitigation of the shielding (Maeda, 2018).

E. Discussion on future strategies to treat cavitation in BWL

In SWL, the long tensile tail can initiate intense cloud cavitation in the focal area. Shortly after the passage of the wave, violent cloud collapse may cause tissue injury (Bailey *et al.*, 2005; Evan *et al.*, 2002; Matlaga *et al.*, 2008). Collapse in the proximity to the stone may also enhance stone comminution (Pishchalnikov *et al.*, 2003). During growth, non-condensable gas diffuses into the bubbles, which causes persistence of nuclei long after the passage of the wave and proliferation of bubble clouds that may cause undesirable energy shielding during the subsequent pulses

(Pishchalnikov *et al.*, 2011; Tanguay, 2004). The BWL waveform, on the other hand, lacks the trailing tensile component, and this results in milder growth of cavitation bubbles compared to those in SWL (Maeda *et al.*, 2015). Bubble clouds are diffuse and do not tend to undergo violent collapse (Maeda and Colonius, 2018a). Strong collapse can lead to fragmentation of bubbles and thus proliferation of bubbles; the absence of it in BWL might enable higher PRF and thus faster treatment than SWL. On the other hand, results of the present study suggest that the more diffuse bubble clouds in BWL still lead to a strong shielding of stones from subsequent pulses and it may be desirable to avoid them. Overall, in BWL, suppressing cloud cavitation using feedback may be an optimal path to achieve both improved safety (May *et al.*, 2017; Movahed *et al.*, 2017) and high efficacy of stone comminution.

In contrast to BWL, there have been proposed prototype methods of HIFU- and histotripsy-based lithotripsy that actively makes use of cloud cavitation for stone comminution (Duryea *et al.*, 2011; Ikeda *et al.*, 2006; Matsumoto and Yoshizawa, 2005; Yoshizawa *et al.*, 2009). Particularly, the HIFU-based method uses HIFU waves with a waveform that alternately combines wave packets of high and low frequencies, called cavitation-control (C-C) waveform, whose effectiveness was demonstrated in experiments *in vitro*. The high- and low-frequency components are designed to excite cloud cavitation on the surface of a stone and trigger violent collapse of the clouds to erode the stone, respectively. Such a multi-frequency strategy could also be applied to BWL for enhancement of stone fragmentation.

We need to recall that, however, cavitation may need precise control such that efficacy and safety are not sacrificed. To date, understanding of cavitation erosion in lithotripsy has remained anecdotal; cavitation bubbles in the vicinity of or attached on a material's surface may cause erosion and fracture of the material due to non-spherical collapse (Crum, 1988; Johnsen and Colonius, 2009; Philipp and Lauterborn, 1998; Zhong *et al.*, 1993), while the underlying physical mechanisms, including fluid-structure interactions and fracture mechanics, have not been fully elucidated. We believe that further understanding of the complex physical mechanisms will be crucial in designing better treatment.

V. CONCLUSION

In this paper, the energy shielding of kidney stones by bubble clouds nucleated on the surface of the stone during the passage of a burst wave was quantified through a combined experimental and numerical approach. Simulated evolution of the bubble cloud and the bubble-scattered acoustics using a compressible, multicomponent flow solver showed quantitative agreement with the results of high-speed photography and acoustic measurements. Results of the simulation revealed that the magnitude of the energy shielding by a thin layer of bubble cloud can reach up to 90% of the total energy of the burst wave that would otherwise be transmitted into the stone, indicating a large potential loss of efficacy of the treatment of BWL due to cloud cavitation. The results extend the previous studies of bubble cloud dynamics in

ultrasound fields (Maeda and Colonius, 2018a; Maeda *et al.*, 2015). Furthermore, we discovered a strong correlation between the magnitude of the shielding and the amplitude of the backscattered acoustics. This correlation could be used, for example, to monitor the magnitude of the shielding in a kidney by measuring the scattered acoustics outside the human body in real time during the treatment of BWL, and adjust parameters to minimize the shielding during a procedure. Future work includes assessment of the effect of the waveform on the energy shielding as well as extension of the combined experimental and numerical setups to model environments *in vivo*.

ACKNOWLEDGMENTS

K.M. would like to acknowledge the Funai Foundation for Information Technology for the Overseas Scholarship. This work was supported by the National Institutes of Health under Grant No. P01-DK043881 and K01-DK104854. The simulations presented here utilized the Extreme Science and Engineering Discovery Environment, which is supported by the National Science Foundation Grant No. CTS120005.

- Bailey, M., McAteer, J., Pishchalnikov, Y., Hamilton, M., and Colonius, T. (2006). "Progress in lithotripsy research," *Acoust. Today* 2(2), 18–29.
- Bailey, M. R., Pishchalnikov, Y. A., Sapozhnikov, O. A., Cleveland, R. O., McAteer, J. A., Miller, N. A., Pishchalnikova, I. V., Connors, B. A., Crum, L. A., and Evan, A. P. (2005). "Cavitation detection during shock-wave lithotripsy," *Ultrasound Med. Biol.* 31(9), 1245–1256.
- Bergamasco, L., and Fuster, D. (2017). "Oscillation regimes of gas/vapor bubbles," *Int. J. Heat Mass Transfer* 112, 72–80.
- Biesheuvel, A., and vanWijngaarden, L. (1984). "Two-phase flow equations for a dilute dispersion of gas bubbles in liquid," *J. Fluid Mech.* 148, 301–318.
- Cash, J., and Karp, A. (1990). "A variable order Runge-Kutta method for initial value problems with rapidly varying right-hand sides," *ACM Trans. Math. Software* 16(3), 201–222.
- Chaigneau, M., and Le, G. M. (1968). "On the composition of gas dissolved in human urine," *C. R. Seances Acad. Sci., Ser. D* 267(22), 1893–1895.
- Coleman, A., Saunders, J., Crum, L., and Dyson, M. (1987). "Acoustic cavitation generated by an extracorporeal shockwave lithotripter," *Ultrasound Med. Biol.* 13(2), 69–76.
- Commander, K., and Prosperetti, A. (1989). "Linear pressure waves in bubbly liquids: Comparison between theory and experiments," *J. Acoust. Soc. Am.* 85(2), 732–746.
- Coralic, V., and Colonius, T. (2014). "Finite-volume WENO scheme for viscous compressible multicomponent flows," *J. Comput. Phys.* 274, 95–121.
- Crum, L. A. (1988). "Cavitation microjets as a contributory mechanism for renal calculi disintegration in ESWL," *J. Urol.* 140(6), 1587–1590.
- Duryea, A. P., Hall, T. L., Maxwell, A. D., Xu, Z., Cain, C. A., and Roberts, W. W. (2011). "Histotripsy erosion of model urinary calculi," *J. Endourol.* 25(2), 341–344.
- Evan, A. P., Willis, L. R., McAteer, J. A., Bailey, M. R., Connors, B. A., Shao, Y., Lingeman, J. E., Williams, J. C., Fineberg, N. S., and Crum, L. A. (2002). "Kidney damage and renal functional changes are minimized by waveform control that suppresses cavitation in shock wave lithotripsy," *J. Urol.* 168(4), 1556–1562.
- Fuster, D., and Colonius, T. (2011). "Modeling bubble clusters in compressible liquids," *J. Fluid Mech.* 688, 352–389.
- Garnier, J., and Papanicolaou, G. (2009). "Passive sensor imaging using cross correlations of noisy signals in a scattering medium," *SIAM J. Imag. Sci.* 2(2), 396–437.
- Hwang, E. Y., Fowlkes, J. B., and Carson, P. L. (1998). "Variables controlling contrast generation in a urinary bladder model," *J. Acoust. Soc. Am.* 103(6), 3706–3716.
- Ikedu, T., Yoshizawa, S., Masataka, T., Allen, J., Takagi, S., Ohta, N., Kitamura, T., and Matsumoto, Y. (2006). "Cloud cavitation control for lithotripsy using high intensity focused ultrasound," *Ultrasound Med. Biol.* 32(9), 1383–1397.
- Johnsen, E., and Colonius, T. (2009). "Numerical simulations of non-spherical bubble collapse," *J. Fluid Mech.* 629, 231–262.
- Kameda, M., and Matsumoto, Y. (1996). "Shock waves in a liquid containing small gas bubbles," *Phys. Fluids* 8(2), 322–335.
- Keller, J., and Miksis, M. (1980). "Bubble oscillations of large amplitude," *J. Acoust. Soc. Am.* 68(2), 628–633.
- Landau, L. D., and Lifshitz, E. M. (1986). *Theory of Elasticity*, vol. 7, Course of Theoretical Physics, 3rd edition (Elsevier, New York).
- Lingeman, J. E., McAteer, J. A., Gnassin, E., and Evan, A. P. (2009). "Shock wave lithotripsy: Advances in technology and technique," *Nat. Rev. Urol.* 6(12), 660–670.
- Maeda, K. (2018). "Simulation, experiments, and modeling of cloud cavitation with application to burst wave lithotripsy," Ph.D. thesis, California Institute of Technology.
- Maeda, K., and Colonius, T. (2017). "A source term approach for generation of one-way acoustic waves in the Euler and Navier-Stokes equations," *Wave Motion* 75, 36–49.
- Maeda, K., and Colonius, T. (2018a). "Bubble cloud dynamics in an ultrasound field," arXiv preprint arXiv:1805.00129.
- Maeda, K., and Colonius, T. (2018b). "Eulerian-Lagrangian method for simulation of cloud cavitation," *J. Comput. Phys.* 371, 994–1017.
- Maeda, K., Kreider, W., Maxwell, A., Cunitz, B., Colonius, T., and Bailey, M. (2015). "Modeling and experimental analysis of acoustic cavitation bubbles for burst wave lithotripsy," *J. Phys. Conf. Ser.* 656(1), 012027.
- Matlaga, B. R., McAteer, J. A., Connors, B. A., Handa, R. K., Evan, A. P., Williams, J. C., Lingeman, J. E., and Willis, L. R. (2008). "Potential for cavitation-mediated tissue damage in shockwave lithotripsy," *J. Endourol.* 22(1), 121–126.
- Matsumoto, Y., and Yoshizawa, S. (2005). "Behaviour of a bubble cluster in an ultrasound field," *Int. J. Numer. Methods Fluids* 47(6-7), 591–601.
- Maxwell, A., Cunitz, B., Kreider, W., Sapozhnikov, O., Hsi, R., Harper, J., Bailey, M., and Sorensen, M. (2015). "Fragmentation of urinary calculi *in vitro* by burst wave lithotripsy," *J. Urol.* 193(1), 338–344.
- Maxwell, A. D., Wang, T.-Y., Cain, C. A., Fowlkes, J. B., Sapozhnikov, O. A., Bailey, M. R., and Xu, Z. (2011). "Cavitation clouds created by shock scattering from bubbles during histotripsy," *J. Acoust. Soc. Am.* 130(4), 1888–1898.
- May, P. C., Kreider, W., Maxwell, A. D., Wang, Y.-N., Cunitz, B. W., Blomgren, P. M., Johnson, C. D., Park, J. S. H., Bailey, M. R., Lee, D., Harper, J. D., and Sorensen, M. D. (2017). "Detection and evaluation of renal injury in burst wave lithotripsy using ultrasound and magnetic resonance imaging," *J. Endourol.* 31(8), 786–792.
- McAteer, J., Bailey, M., Williams, J., Jr., Cleveland, R., and Evan, A. (2005). "Strategies for improved shock wave lithotripsy," *Minerva Urol. Nefrol.* 57(4), 271–287.
- Miller, D. L., Smith, N. B., Bailey, M. R., Czarnota, G. J., Hynynen, K., Makin, I. R. S., and Bioeffects Committee of the American Institute of Ultrasound in Medicine. (2012). "Overview of therapeutic ultrasound applications and safety considerations," *J. Ultrasound Med.* 31(4), 623–634.
- Movahed, P., Kreider, W., Maxwell, A., Dunmire, B., and Freund, J. (2017). "Ultrasound-induced bubble clusters in tissue-mimicking agar phantoms," *Ultrasound Med. Biol.* 43(10), 2318–2328.
- Okita, K., Sugiyama, K., Takagi, S., and Matsumoto, Y. (2013). "Microbubble behavior in an ultrasound field for high intensity focused ultrasound therapy enhancement," *J. Acoust. Soc. Am.* 134(2), 1576–1585.
- Otsu, N. (1979). "A threshold selection method from gray-level histograms," *IEEE Trans. Syst. Man Cybern.* 9(1), 62–66.
- Perigaud, G., and Saurel, R. (2005). "A compressible flow model with capillary effects," *J. Comput. Phys.* 209(1), 139–178.
- Philipp, A., and Lauterborn, W. (1998). "Cavitation erosion by single laser-produced bubbles," *J. Fluid Mech.* 361, 75–116.
- Pishchalnikov, Y. A., McAteer, J. A., Williams, J. C., Jr., Pishchalnikova, I. V., and Vonderhaar, R. J. (2006). "Why stones break better at slow shock-wave rates than at fast rates: *In vitro* study with a research electrohydraulic lithotripter," *J. Endourol.* 20(8), 537–541.
- Pishchalnikov, Y., Sapozhnikov, O., Bailey, M., Williams, J., Jr., Cleveland, R., Colonius, T., Crum, L., Evan, A., and McAteer, J. (2003). "Cavitation bubble cluster activity in the breakage of kidney stones by lithotripter shockwaves," *J. Endourol.* 17(7), 435–446.
- Pishchalnikov, Y. A., Williams, J. C., Jr., and McAteer, J. A. (2011). "Bubble proliferation in the cavitation field of a shock wave lithotripter," *J. Acoust. Soc. Am.* 130(2), EL87–EL93.

- Poynton, C. (2012). *Digital Video and HD: Algorithms and Interfaces* (Elsevier, Boston, MA).
- Preston, A., Colonius, T., and Brennen, C. (2007). "A reduced-order model of diffusive effects on the dynamics of bubbles," *Phys. Fluids* **19**, 123302.
- Stride, E., and Coussios, C. (2010). "Cavitation and contrast: The use of bubbles in ultrasound imaging and therapy," *Proc. Inst. Mech. Eng. H* **224**(2), 171–191.
- Tanguay, M. (2004). "Numerical simulation and analysis of shockwave lithotripsy," Ph.D. thesis, California Institute of Technology.
- Thoma, C. (2014). "Stones: Bursting through limitations of SWL," *Nat. Rev. Urol.* **11**(10), 540.
- Wang, Y.-C., and Brennen, C. (1999). "Numerical computation of shock waves in a spherical cloud of cavitation bubbles," *J. Fluids Eng.* **121**(4), 872–880.
- Yoshizawa, S., Ikeda, T., Ito, A., Ota, R., Takagi, S., and Matsumoto, Y. (2009). "High intensity focused ultrasound lithotripsy with cavitating microbubbles," *Med. Biol. Eng. Comput.* **47**(8), 851–860.
- Yura, T., Lafond, M., Yoshizawa, S., and Umemura, S.-I. (2018). "Effect of annular focusing of ultrasound on rate of stone erosion using cavitation bubbles," *Jpn. J. Appl. Phys.* **57**(7S1), 07LB18.
- Zhong, P., Chuong, C., and Preminger, G. (1993). "Propagation of shock waves in elastic solids caused by cavitation microjet impact. II: Application in extracorporeal shock wave lithotripsy," *J. Acoust. Soc. Am.* **94**(1), 29–36.